EARTH SURFACE PROCESSES AND LANDFORMS
*Earth Surf. Process. Landforms* **43**, 134–149 (2018)

Published online 9 May 2017 in Wiley Online Library
(wileyonlinelibrary.com) DOI: 10.1002/esp.4158

# Observations on sandbar behaviour along a man-made curved coast

**J. Rutten,*** **B. G. Ruessink** **and T. D. Price**
Department of Physical Geography, Faculty of Geosciences, Utrecht University, 3508 TC Utrecht, The Netherlands

Received 20 October 2016; Revised 24 February 2017; Accepted 28 March 2017

*Correspondence to: J. Rutten, Department of Physical Geography, Faculty of Geosciences, Utrecht University, 3508 TC Utrecht, The Netherlands. E-mail: j.rutten@uu.nl


ESPL
Earth Surface Processes and Landforms

ABSTRACT: Sandbars, submerged ridges of sand parallel to the shoreline, affect surfzone circulation, beach topography and beach width. Under time-varying wave forcing, sandbars may migrate onshore and offshore, referred to as two-dimensional (2D) behaviour, and vary in planshape from alongshore uniform ridges to alongshore non-uniform ridges through the growth and decay of three-dimensional (3D) patterns, referred to as 3D behaviour. Although 2D and 3D sandbar behaviour is reasonably well understood along straight coasts, this is not the case for curved coasts, where the curvature can invoke spatial variability in wave forcing. Here, we analyse sandbar behaviour along the ~ 3000 m man-made curved coastline of the Sand Engine, Netherlands, and determine the wave conditions governing this behaviour. 2D and 3D behaviour was quantified within a box north and west of the Sand Engine's tip, respectively, using a 2.4-year dataset of daily low-tide video images and a sparser bathymetric dataset. The northern and western sides behaved similarly in terms of 2D behaviour, with seasonal onshore and offshore migration, resulting in a stable position on inter-annual timescales. However, both sandbar geometry and 3D behaviour differed substantially between both sides. The geometric differences (bar shape, bar crest depth and wavelength of 3D patterns) are consistent with computed alongshore differences in breaker height due to refraction. The differences in the timing in growth, decay and morphological coupling of 3D patterns in the sandbar and shoreline are likely related to differences in the local wave angle, imposed by the curved coast. Similar dependency of bar behaviour on local wave height and angle may be expected elsewhere along curved coasts, e.g. shoreline sandwaves, cuspate forelands or embayed beaches. Copyright © 2017 John Wiley & Sons, Ltd.

KEYWORDS: surfzone morphology; nearshore sandbars; mega-nourishment; alongshore variability; video analysis

## Introduction

Sandbars are shallow submerged ridges parallel to the shoreline that characterize many wave-dominated beaches throughout the world. These features, forming the first line of natural coastal defence against storm waves, have a dynamic character that has intrigued the nearshore scientific community for decades. Today, we have a reasonable understanding why sandbars migrate slowly onshore under calm wave conditions and rapidly offshore under more energetic conditions (e.g. Thornton and Humiston, 1996; Gallagher *et al.*, 1998; Elgar *et al.*, 2001; Hoefel and Elgar, 2003). Additionally, many studies (Sonu, 1973; Wright and Short, 1984; Lippmann and Holman, 1990; Van Enckevort and Ruessink, 2003) have investigated the growth and decay of seaward and shoreward protrusions in cross-shore sandbar position, resulting in a three-dimensional (3D) geometry with alongshore variability in depth and cross-shore position and in a two-dimensional (2D), alongshore-uniform sandbar geometry, respectively. The protrusions generally tend to form under calm conditions after storms or in the summer season, and tend to disappear under high waves (Wright and Short, 1984) or under obliquely incident waves driving a strong alongshore current (Price and Ruessink, 2013; Contardo and Symonds, 2015). Although numerous studies examined sandbar behaviour along straight coasts, both in natural systems (Lippmann and Holman, 1990; Van Enckevort and Ruessink, 2003) and human-disturbed systems (Grunnet and Ruessink, 2005; Ojeda *et al.*, 2008), sandbar behaviour along strongly curved coasts has received less attention and is thus not well understood. Nowadays, insight into the effect of a curved coast on system behaviour is demanded with the recent shift in nourishment policy towards large-scale and long-term measures that serve on decadal timescales over kilometres of coast (see Stive *et al.*, 2013). Kilometre-scale perturbations in the coastline, intended to feed the adjacent beach or to reinforce the coastal strip, have recently been constructed to keep up the current coastal safety levels in view of rising sea levels due to climate change and continuing coastal erosion (Stive *et al.*, 2013; Wong *et al.*, 2014). An example of such a perturbation is the Sand Engine, a concentrated feeder nourishment in the Netherlands (De Schipper *et al.*, 2016). Initially, the nourishment protruded 1 km into the sea and extended 3 km alongshore, resulting in a strongly curved coast with varying coastline orientation with respect to the offshore wave conditions. Observations suggest that this curvature affected the behaviour of the newly developed sandbars along the perturbation (e.g. Chong, 2014). The sandbar planshapes varied from alongshore-variable (3D)

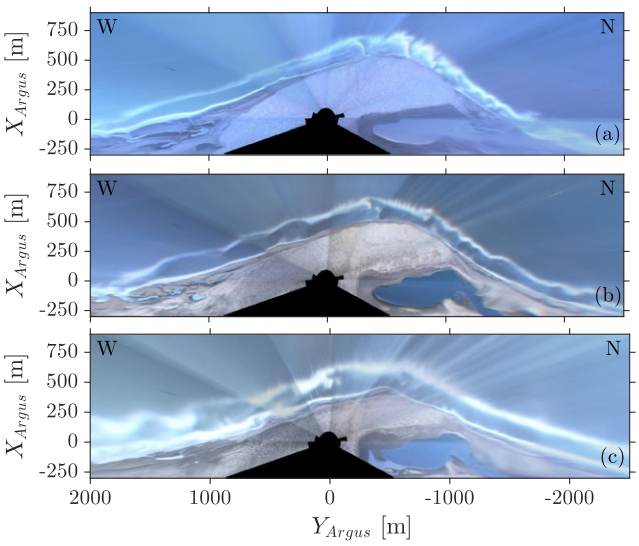


**Figure 1.** Examples of plan view images on (a) 4 June 2013, (b) 23 November 2013 and (c) 24 January 2015, illustrating the dynamics of the sandbar and shoreline morphology along the convex coastline of the Sand Engine. [Colour figure can be viewed at wileyonlinelibrary.com]

along the entire perturbation (Figure 1b) to dissimilar configurations at both sides of the perturbation (Figure 1a, c).

Analogues of barred curved coasts can be found in natural systems. Convex analogues comprise shoreline sandwaves and cuspate forelands, whereas embayed beaches form concave analogues. Few studies concern sandbar behaviour along convex coasts. Stewart and Davidson-Arnott (1988) and Davidson-Arnott and Van Heyningen (2003) found that the welding of sandbars to the beach resulted in the generation, growth and alongshore migration of longshore sandwaves (wavelength of 500–2500 m, lifetime of 5–10 years) along Long Point spit (Lake Erie), Canada. On the downdrift side of these sandwaves, they observed rhythmic inner bars to migrate onshore and eventually weld to the beach. No observations were reported on sandbar behaviour at the updrift side. The observed bar behaviour was attributed to both sediment abundance in the inner nearshore zone and to low, obliquely incident waves in spring and summer. Aagaard and Kroon (2007) found opposite long-term bar behaviour along the two flanks of a cuspate foreland, Blåvands Huk, Denmark. Net offshore migration was observed where the profile had a relatively steep shoreface (1:210, between −7 and 0 m with respect to mean sea level (MSL)) with pronounced (up to 3 m) sandbars, whereas net onshore migration was observed where the shoreface profile was more gentle (1:370). Model simulations suggested that seaward transport due to strong undertow currents dominated over the steep profile with a pronounced bar morphology, whereas shoreward transport due to wave skewness dominated over the gentle profile with less voluminous sandbars. Opposite fluxes in littoral drift may also have contributed to inter-site differences in either shoreface profile or bar behaviour itself. Backstrom *et al.* (2008) found alongshore differences in morphological response across the shoreface of a cuspate delta, southern Spain, from a pre-storm and post-storm bathymetric survey. Minor change in sandbar morphology was observed along the eastern side where waves arrived shore-normally, whereas substantial change was recorded within the double bar system along the southern side where waves arrived obliquely. They were inconclusive whether alongshore currents or rip currents drove the morphological change of the double bar system at the southern side.

Although concave beaches are more abundant and have received more attention than convex beaches, the alongshore differences in sandbar behaviour have not often been the subject of study. However, some observations have been made along the concave coast of embayed beaches, enclosed by one or two headlands, bluffs or man-made structures. Short (1978) and Wright and Short (1984) observed an alongshore gradient in modal beach state along the embayment of Fisherman's-Collaroy-Narrabeen, Australia, from reflective at Fisherman's, associated with low energetic conditions, through low-tide-terrace and transverse-bar-rip at Collaroy, to rhythmic-bar-beach at Narrabeen, associated with moderate energetic conditions (Short, 1978, his Figure 7; Wright and Short, 1984, their Figure 8). Along Monterey Bay, USA, a similar energy gradient in modal beach state was reported by Thornton *et al.* (2007), from reflective states in the southern end of the embayment to intermediate states halfway along the embayment. Such energy gradients can be explained by the geometry of the embayment and the wave conditions. An alongshore gradient in breaker wave height arises under obliquely incident waves due to shadowing effects by one of the headlands. As a result, embayments that are exposed to a wave climate with predominantly oblique waves tend to have an alongshore gradient in wave energy, and thus in modal beach state. Besides an alongshore gradient in breaker wave height, the embayment geometry may also induce alongshore differences in wave refraction, diffraction and reflection. Such alongshore differences lead to an alongshore gradient in wave angle that may further contribute to an alongshore variation in modal beach state. To illustrate, model simulations of Tairua Beach (Gallop *et al.*, 2011) and Bondi Beach (McCarroll *et al.*, 2016) – two embayments with a longshore variation in bar morphology – revealed an alongshore gradient in wave energy, arising from asymmetric geological boundary conditions at both sites. At Tairua Beach a nearby island resulted in wave shadowing, and at Bondi Beach one of the headlands and a subaqueous reef locally reduced wave heights. Besides a modal state, alongshore variability in 2D and 3D sandbar morphology may change with time-varying wave conditions, depending on the responsiveness of the system. For shoreline datasets, for example, interannual (Ojeda *et al.*, 2011; Ranasinghe *et al.*, 2004a), seasonal Harley *et al.* (2015) and event (Van de Lageweg *et al.*, 2013) signals in alongshore variable 2D and 3D behaviour were found. Similarly, sandbar behaviour may vary alongshore, as found by Gallop *et al.* (2011) and McCarroll *et al.* (2016), showing that a sandbar migrated offshore under storm conditions at the exposed side of the beach only. In addition, Blossier *et al.* (2016) and Ojeda *et al.* (2011) reported on the rotation of a sandbar due to longshore differences in 2D behaviour, similar to beach rotation (e.g. Harley *et al.*, 2015). Different to the convex examples, embayed beaches have physical lateral boundaries that potentially limit alongshore exchange of sand outside the system, promote trapping of sand within the system (i.e. beach rotation) and control headland rip formation. Moreover, the concave shape creates a gradual alongshore change in local wave forcing, whereas the local wave forcing along a convex coastline changes rather abruptly across its most seaward protruding point.

On a kilometre scale, the behaviour of convex coasts (e.g., sandwaves) or concave coasts (e.g., beach rotation) themselves have been studied extensively. The superimposed morphological meso-scale features ($O$(10–100 m)), such as sandbars, may importantly affect the underlying, large-scale morphodynamics (e.g. Stewart and Davidson-Arnott, 1988; Harley *et al.*, 2015). However, the meso-scale behaviour along curved coasts remains relatively unknown. Studies on sandbar behaviour at concave coasts mainly examined temporal variability in beach states (Wright and Short, 1984;

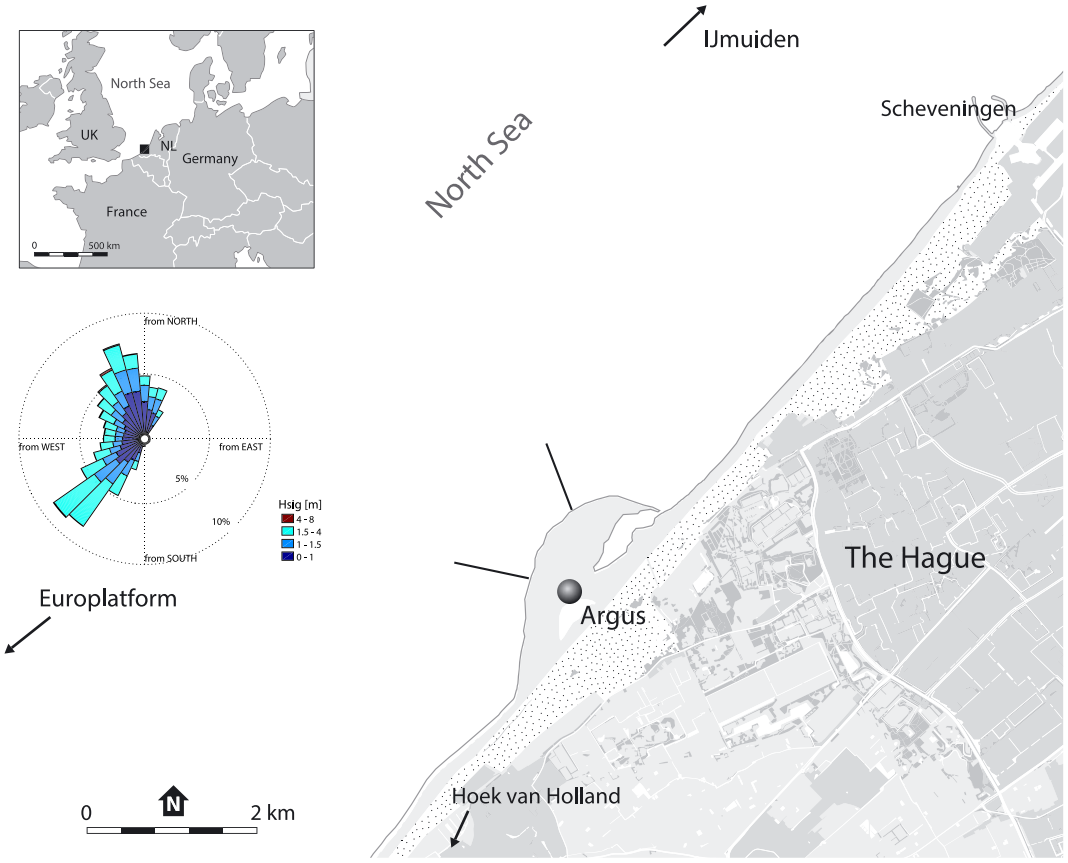


**Figure 2.** Study site. Depth contours are roughly parallel to the coast, and contracted (until 10 m depth) at the perturbation. The black lines at the Sand Engine show the transects of the profiles shown in Figure 6. The wave rose shows offshore wave measurements for the period 2005–2015. The dots depict the dunes, whereas the greyish colours inland represent built-up areas. [Colour figure can be viewed at wileyonlinelibrary.com]

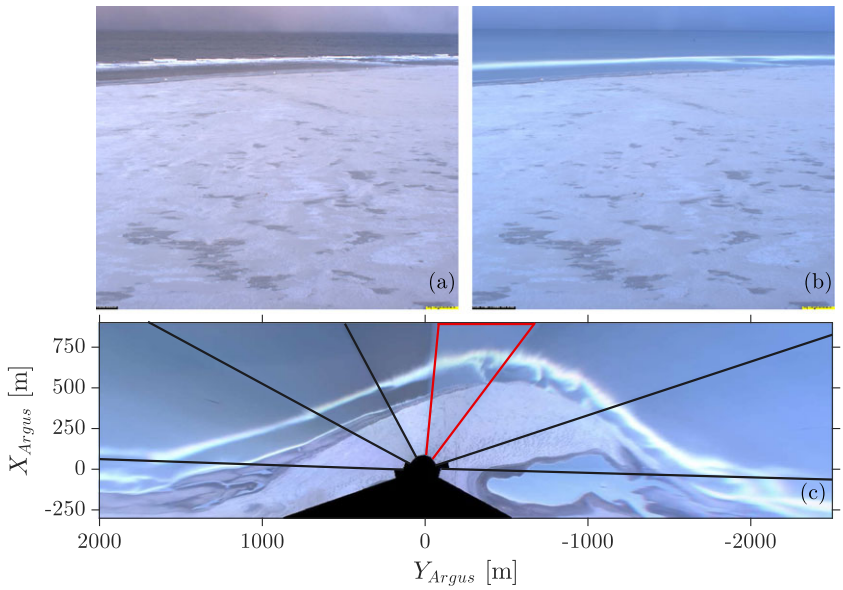


**Figure 3.** Example of (a) snapshot, (b) 10 min time-exposure image and (c) planview. The black lines in (c) represent the camera seams, where the red delineated part corresponds to the time-exposure image shown in (b). [Colour figure can be viewed at wileyonlinelibrary.com]

Ranasinghe *et al.*, 2004b), morphological coupling (Van de Lageweg *et al.*, 2013) and rip channels or 3D bar morphology (Holman *et al.*, 2006; Splinter *et al.*, 2011; Ojeda *et al.*, 2011). The spatial variability herein received minor attention, especially bar behaviour at daily to seasonal timescales. Moreover, the few studies addressing sandbar behaviour along convex coasts were based on datasets with low temporal resolution or of short duration. Herein, we use a 2.4-year dataset of daily low-tide, 10 min averaged Argus video images (Holman and Stanley, 2007), collected from the convex, curved coast of the Sand Engine, which offers the unique opportunity for studying bar behaviour along a convex coastline. The aim of this paper was (1) to describe the spatiotemporal variability in sandbar behaviour along the convex curved coast of the Sand

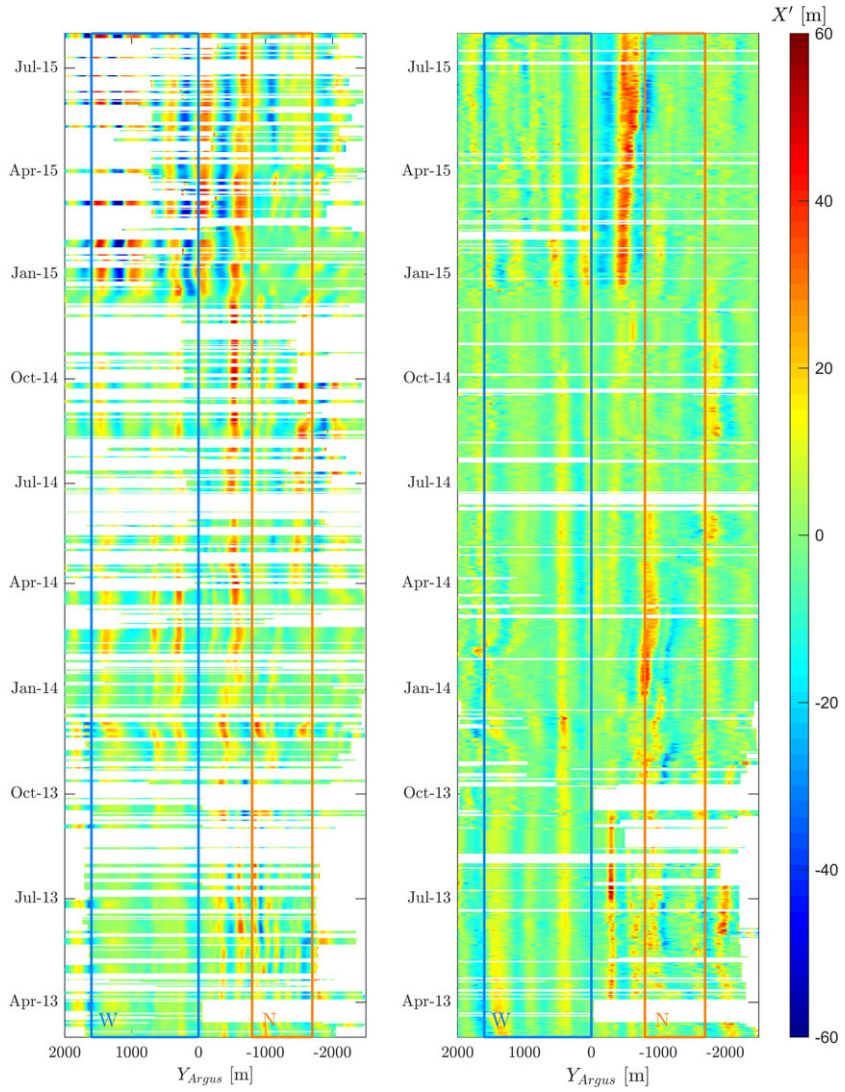


**Figure 4.** Timestack of perturbations in the barline $X_b'$ (left) and MWL line $X_s'$ (right). The boxes indicate how the study area was divided into a north (N) and west (W) side that were used for morphometric computations. Red (warm) and blue (cold) colours correspond to seaward and shoreward perturbations, respectively. White parts represent no data. [Colour figure can be viewed at wileyonlinelibrary.com]

Engine at daily to seasonal timescales and (2) to determine the wave conditions governing this behaviour. First, we describe the study site, dataset and analysis methods. Then, we present our results on sandbar behaviour, preceded by a subsection on large-scale evolution of the Sand Engine since its construction. This is followed by a discussion on the wave field and resulting wave-induced currents governing the observed sandbar behaviour, particularly focusing on the breaker wave height and the wave angle. Finally, we provide the main conclusions of our work.

## Methodology

### Study site

The study was performed at the 21.5 $Mm^3$ Sand Engine, a concentrated sand nourishment along the southwest–northeast (42° with respect to the north) oriented Delfland coast, Netherlands (Figure 2). The Sand Engine was constructed in summer 2011 with the aim of feeding the beaches of the erosive Delfland coast under predicted sea level rise, in a more efficient and environmentally friendly form than traditional nourishments placed locally at the beach or at the shoreface (Stive *et al.*, 2013). The peninsula consists of sediments with an average $D_{50}$ of $\sim 280\mu$m (De Schipper *et al.*, 2016), slightly coarser than the median grain size $\sim 250\mu$m (Wijnberg and Terwindt, 1995) before construction of the Sand Engine.

The study site is exposed to a bimodal wave climate, with waves predominantly from the southwest (222° N) or north-northwest (347° N; Figure 2). The yearly-averaged offshore significant wave height $H_{m0}$ is 1.3 m, with a yearly-averaged peak period $T_p$ of 5.7 s. Typically, $T_p$ increases with $H_{m0}$, and is largest for waves from the northwest, which have the largest fetch. Summer (April–September) is characterized by low waves ($H_{m0} = 1.1$ m), whereas storms ($H_{m0}$ up to 5 m) dominate the autumn and winter season (September–April). The semi-diurnal tide imposes a tidal range of 1.7 m and drives a tidal current parallel to the shore with peak velocities of about 0.5 m $s^{-1}$. The wave climate, in particular in relation to the observations on sandbar and shoreline behaviour, is further analysed in the Discussion.

### Image and field data

A 2.4-year dataset of daily video images was collected by an Argus video station, between March 2013 and July 2015. Eight 5.0 megapixel cameras, 42.7 m above mean sea level (MSL)

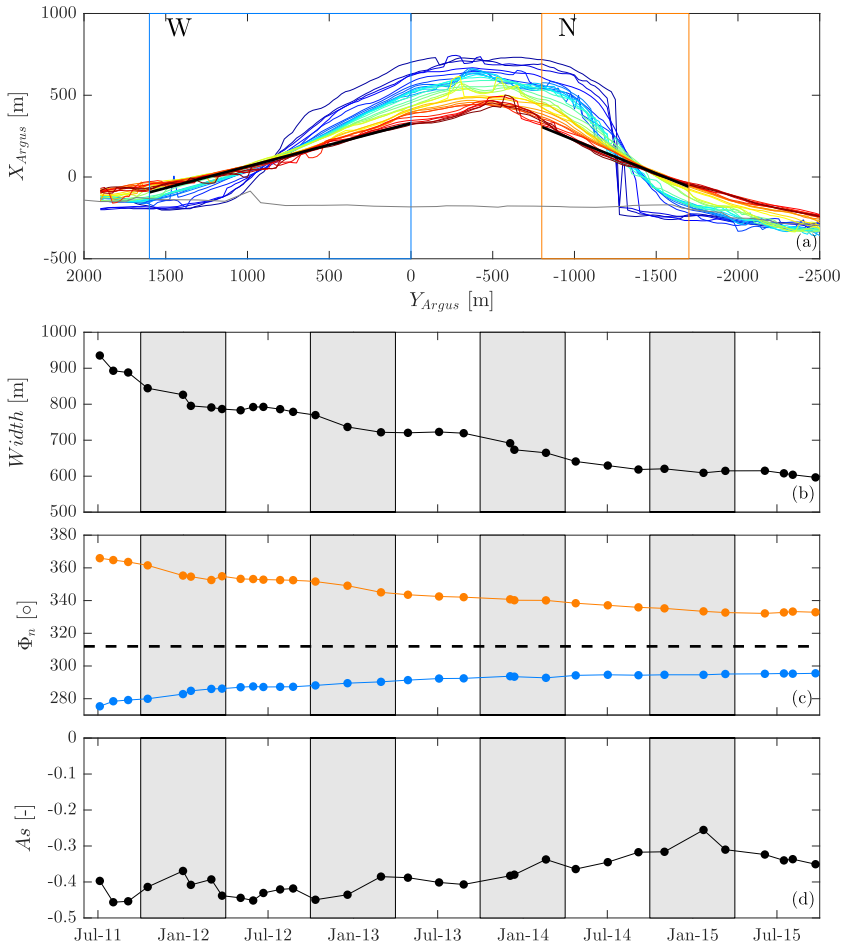


**Figure 5.** The gradual diffusion of the Sand Engine is illustrated by the (a) −1 m contours from August 2011 (blue) until July 2015 (red), (b) the maximum cross-shore extension of the −1 m contour with respect to the pre-nourishment situation, and (c) the orientation of the shore-normal $\Phi_n$ at the northern (orange) and western (blue) side. The black lines in (a) depict the linear fit performed on every contour at the northern and western side to estimate $\Phi_n$. The jump in the first (i.e. blue) contour lines at $Y_{\text{Argus}} = -1300$ m is caused by the initially wide lagoon entrance of the Sand Engine. The black dashed line in (c) denotes an orientation of 312° similar to the pre-nourishment situation. The temporal evolution of the asymmetry *As* of the −1 m contour is shown in (d), where negative values reflect a contour that pitches northward and zero asymmetry reflects a symmetric plan shape. The grey shading in (b), (c) and (d) indicates the winter months. [Colour figure can be viewed at wileyonlinelibrary.com]

mounted atop a tower, recorded 245° of the horizontal plane. The images of the eight cameras were rectified and merged to a single plan view image (Figure 3) using two inverted photogrammetric equations (Holland *et al.*, 1997) with input on the camera position, camera orientation (tilt, pitch, roll) and focal length. The orientation of each camera was calculated using ground control points (GCPs) on the beach that were within the field of view and of which the coordinates were known. After an initial set of camera orientations based on temporary GCPs, camera orientations changed slightly due to strong wind or thermal expansion, and thus the orientations were updated regularly when GCPs were within the view of the camera (cameras 1, 2, 3, 4, 7, 8). Focal length, field of view and the correction for radial lens distortion were determined in the laboratory. The eight images were projected on the local Argus coordinate system, with the *x*-axis directed offshore, the *y*-axis directed to the southwest (220°) along the beach and *z* constant at the tidal level. The images covered 1200 m in the cross-shore and 4500 m in the alongshore direction, and had a grid resolution of 2 × 2 m. Pixel footprints increased from 0.03 × 0.2 m at 200 m to 0.2 × 1.2 m at 1000 m from the Argus station. For this study, we used 778 10 min time exposure (Timex) images. In these images the individual waves are averaged out; instead, white, alongshore coherent lines can be distinguished as a result of time-averaged wave breaking over the shallow sandbars (Lippmann and Holman, 1989; Van Enckevort and Ruessink, 2001; Figure 3). Figure 1 shows examples of such breaker lines at our study site, varying in both space and time, from straight at either the northern and/or western side to undulating lines, with seaward and shoreward protrusions, at any of the sides. The images show two breaker lines, where the seaward (outer) line serves as proxy for the sandbar and the shoreward (inner) line represents the shoreline. In the Appendix we show that the video-derived position resembles the *in situ* measured bar crest or shoreline with an accuracy of *O*(10 m), consistent with Van Enckevort and Ruessink (2001), Plant *et al.* (2007) and Ribas *et al.* (2010). Both breaker lines, hereafter referred to as barline and shoreline, were extracted with a semi-automatic algorithm that finds the cross-shore pixel intensity maximum for each alongshore position in the images (Pape *et al.*, 2010). Some days no barline and/or shoreline could be detected due to camera failure, fog or the lack of breaking waves during low-energetic conditions. Breaker lines shift onshore under an increased water level. Therefore, only low-tide images were considered, to reduce the tide-induced shifting of both breaker lines (Van Enckevort and Ruessink, 2001). In addition, the shoreline was translated to −0.68 m MSL, i.e. mean low water (MLW), to remove wave- and tide-induced shifting (see Appendix).

The sets of barlines $x_b(y, t)$ and shorelines $x_s(y, t)$ were filtered for lengths smaller than 750 m using a scale-controlled quadratic loess filter (Plant *et al.*, 2002). The resulting two sets,

$X_b(y,t)$ and $X_s(y,t)$, contain large length scales (the shape of the Sand Engine) and lack small length scales (perturbations in the sandbar and shoreline). Both $X_b(y,t)$ and $X_s(y,t)$ were subtracted from $x_b(y,t)$ and $x_s(y,t)$ and filtered for lengths smaller than of interest to us (i.e. < 75 m), resulting in two sets that contain only the perturbations in the barline and shoreline $X_b'(y,t)$ and $X_s'(y,t)$.

Figure 4 shows that $X_b'(y,t)$ and $X_s'(y,t)$ varied in time from 2D (e.g. July 2013 between $y = 0$ m and $y = 2000$ m) to strongly 3D (e.g. December 2013 between $y = 0$ m and $y = 2000$ m), but they also varied alongshore. Perturbations at the western side did not necessarily arise or occur simultaneously at the northern side; see, for example, January 2015. Moreover, the length scale of the perturbations was different: note the alongshore differences in June 2013. To analyse the differences in sandbar and shoreline behaviour along the curved coastline of the Sand Engine, we divided the coast into two sides (north and west) that have an approximately straight coastline and exhibit a similar development of patterns in Figure 4. Since the 3D patterns hardly migrated along the tip from the northern to the western side or vice versa (Figure 4), we treat the two sides as mutually independent in the analyses and interpretation of our results.

Hourly measurements of significant wave height $H_{m0}$, peak wave period $T_p$ and mean wave direction with respect to the north $\theta_N$ were obtained from two offshore stations: the Europlatform (EUR) wave buoy, located in 32 m water depth at 63 km west of the field site, and the wave buoy at IJmuiden Munitiestortplaats (IJM), located in 21 m water depth 56 km north of the field site. Wave information was used from EUR for W–S waves ($\theta_N \leq 280°$), 47% of the time, and from IJM for W–N waves ($\theta_N > 280°$), 38% of the time. When no measurements were available for the preferred station (3%, 10% and 4% of the time for $H_{m0}$, $\theta_N$, and $T_p$ respectively), wave information was used from the other station. No wave measurements were available at either of the stations for 15% of the time. For this study, offshore wave characteristics were transferred to wave characteristics at 10 m water depth, using a wave lookup table (https://publicwiki.deltares.nl/display/BWN1/Tool+Wave+Transformation+Table, accessed most recently in September 2016). Accordingly, for our 2.4-year study period the mean $H_{m0}$ reduced from 1.3 m to 0.97 m and the two directional modes changed from 222° to 258° and from 347° to 338° due to wave refraction.

## Morphometric parameters

To quantify the sandbar and shoreline behaviour, three morphometric parameters were computed: mean position $\mu$ of $X(y,t)$, standard deviation $\sigma$ of $X'(y,t)$ as a measure of three-dimensionality, and cross-correlation between $X_b'(y,t)$ and $X_s'(y,t)$ to quantify a potential morphological coupling (Van Enckevort and Wijnberg, 1999; Ruessink *et al.*, 2007; Price and Ruessink, 2013; Van de Lageweg *et al.*, 2013). Here, we computed the lagged cross-correlation $r$ between two signals $x(n,t)$ and $y(n,t)$ as follows:

$$r(m,t) = \frac{\mathrm{cov}_{xy}(m,t)}{\sqrt{\mathrm{cov}_{xx}(0,t)\mathrm{cov}_{yy}(0,t)}} \tag{1}$$

where $\mathrm{cov}_{xy}(m,t)$ is the covariance function of $x(n,t)$ shifted over lag $m$ and $y(n,t)$ at time $t$:

$$\mathrm{cov}_{xy}(m,t) = x(n+m,t)y(n,t) - \overline{x(t)y(t)} \tag{2}$$

with $n = 0 \ldots N$, $m = -N+1 \ldots N-1$, and $N$ the total number of points. $r$ can vary between −1 or maximum negatively correlated, through 0 or uncorrelated to 1 or maximum positively correlated. In this study, an $r$ towards 1 implies that $X_b'(y,t)$ and $X_s'(y,t)$ show exactly the same pattern, referred to as coupled in phase, whereas an $r$ towards −1 implies that patterns are exactly opposite, referred to as out of phase (Castelle *et al.*, 2010). A maximum in $r$ at positive lag $m$ indicates that the correlated patterns in $X_s'(y,t)$ have an offset to the south (left in the image) with respect to $X_b'(y,t)$, whereas a negative lag $m$ denotes an offset to the north. The 98% confidence interval of significant cross-correlation was computed using the method of Garrett and Toulany (1981), following Price and Ruessink (2013).

For further analysis of morphological coupling, only barlines and shorelines were included that had a certain alongshore variability, $\sigma(X_s') > 7$ m and $\sigma(X_b') > 7$ m, following Price and Ruessink (2013).

## Forcing parameters

To determine the wave conditions that govern the observed sandbar behaviour, three forcing parameters were computed: wave power, alongshore wave power and breaker wave height.

Wave power $P$ was computed as

$$P = \frac{\rho g^2}{32\pi} H_{\mathrm{rms},10}^2 T_{p,10} \tag{3}$$

with sea water density $\rho$ of 1025 kg m$^{-3}$, gravitational acceleration $g$ of 9.81 m s$^{-2}$, root-mean-square wave height $H_{rms,10}$ and peak period $T_{p,10}$, both at 10 m water depth. Here, $P$ is a measure for the offshore wave energy imposed on the sandbar system. Its alongshore component, the alongshore wave power $P_y$, following Komar (1976) and Price and Ruessink (2011), was computed as

$$P_y = P \sin\theta_{10} \cos\theta_{10} \tag{4}$$

with the wave angle at 10 m water depth $\theta_{10}$. Breaker wave height $H_b$, following Komar (1976) and Splinter *et al.* (2011), was computed as

$$H_b = \left(\frac{0.42}{g}\right)^{1/5} \left(H_{\mathrm{rms},10}^2 c_{g,10} \frac{\cos\theta_{10}}{\cos\theta_b}\right)^{2/5} \tag{5}$$

with group velocity at 10 m depth $c_{g,10}$, and wave angle at breaking $\theta_b$.

Here, $P_y$ and $H_b$ were estimated for both the northern and western side, by taking $\theta_{10}$ with respect to the shore-normal at either side, where $\theta_b$ was assumed to be 0° for both sides. To account for the typical slow and delayed response of the morphology to changes in the wave forcing, smoothed time series were created of both $P$ and $P_y$ by averaging over the eight preceding days, following Quartel *et al.* (2008). Furthermore, for $H_b$ the 2.4-year dataset averages were computed to evaluate the averaged imposed wave energy at the northern and western side.

# Results

## Large-scale evolution

To illustrate how the large-scale morphology of the Sand Engine has evolved since the Sand Engine's construction in 2011, we first describe the development of the planshapes (Figure 5) and the cross-shore profiles (Figure 6), based on bed

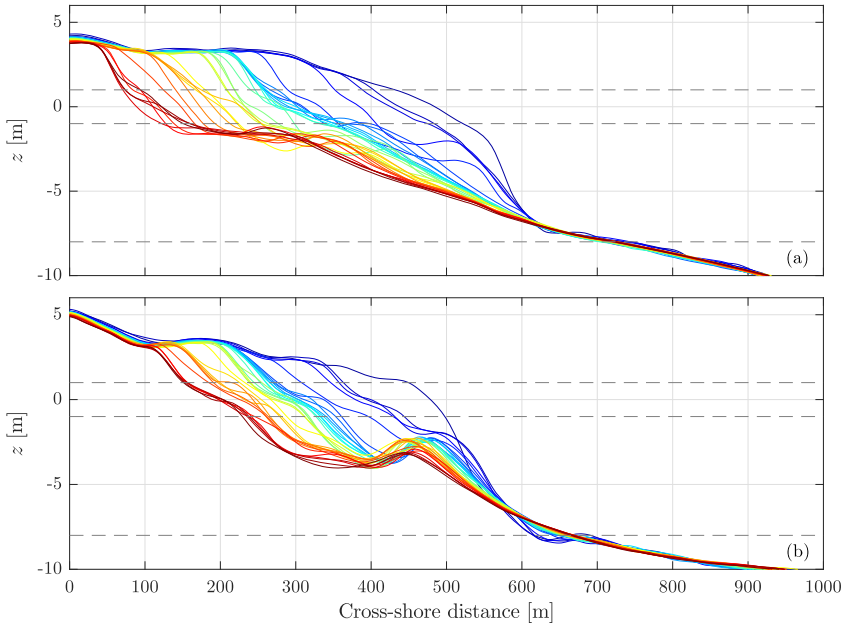


**Figure 6.** Cross-shore profiles of bed elevation $z$ from July 2011 (blue) until June 2015 (red) at a location representative for the northern side (a) and the western side (b). The grey dashed lines indicate +1 m MSL, −1 m MSL and −8 m MSL, used to estimate the cross-shore slope (see Figure 7). Profiles were extracted from *in situ* measurements, collected every 1–3 months (collection moments can be interpreted from the dots in Figure 5b–d). [Colour figure can be viewed at wileyonlinelibrary.com]

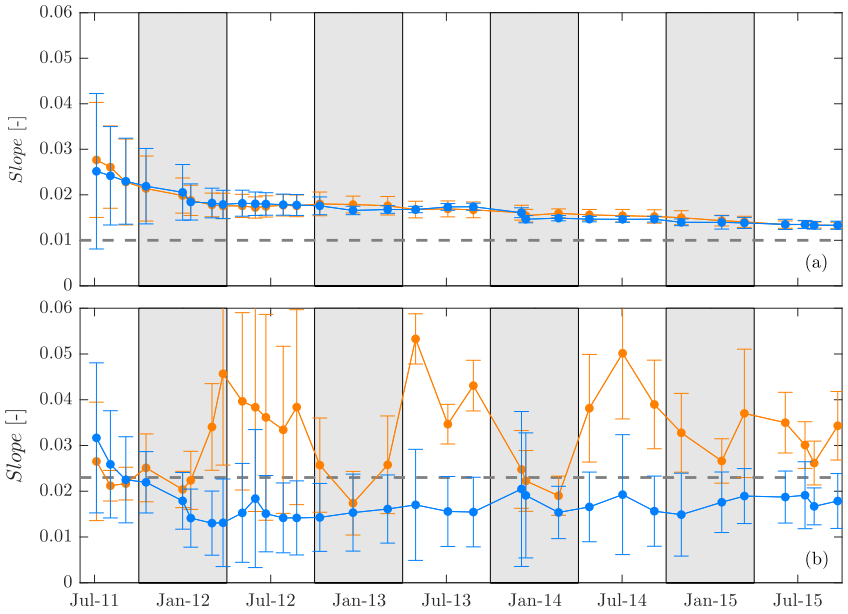


**Figure 7.** The cross-shore slope between (a) −1 m MSL and −8 m MSL, and (b) −1 m MSL and +1 m MSL, averaged alongshore at the northern (orange) and the western (blue) side. Error bars indicate the standard deviation in cross-shore slope at the northern and western side. The grey dashed line indicates the slope before construction of the Sand Engine. The grey shading indicates the winter months. [Colour figure can be viewed at wileyonlinelibrary.com]

elevations measured *in situ* by jetski. Every 2–3 months data were collected along cross-shore transects separated by 80 m (refined to 40 m, shoreward of the −7 m contour). We refer to De Schipper *et al.* (2016), who focused only on the first year of the Sand Engine's large-scale evolution, for details on the data collection.

The Sand Engine was constructed as a strongly curved protrusion of the natural coastline to stimulate the erosion and diffusion of the nourished sand to the adjacent beaches through wave, tidal and wind forces. Indeed, the nourishment itself lost 1.5 $Mm^3$ of sand within 1 year after completion, while the northeastern and southwestern adjacent coasts gained 0.7 $Mm^3$ and 0.5 $Mm^3$, respectively (De Schipper *et al.*, 2016). This diffusion (ongoing; for long-term predictions see Arriaga *et al.*, 2017) can be explained by the gradients in net alongshore sand transport induced by the curved coast. Given the high longshore transport rates, a spit developed at the northern end of the nourishment where the coast was initially strongly curved, and it continued to grow towards the northward located beach (Figure 1). The diffusion of the Sand Engine is reflected in the decreasing curvature of the −1 m contour (Figure 5a), in the decreasing maximum cross-shore width of the nourishment (Figure 5b), as well as in the orientation of the −1 m contour, $\Phi$, at the northern and western side. The two orientations, computed as the gradient of a linear fit through the −1 m contour over the northern and western side, respec-

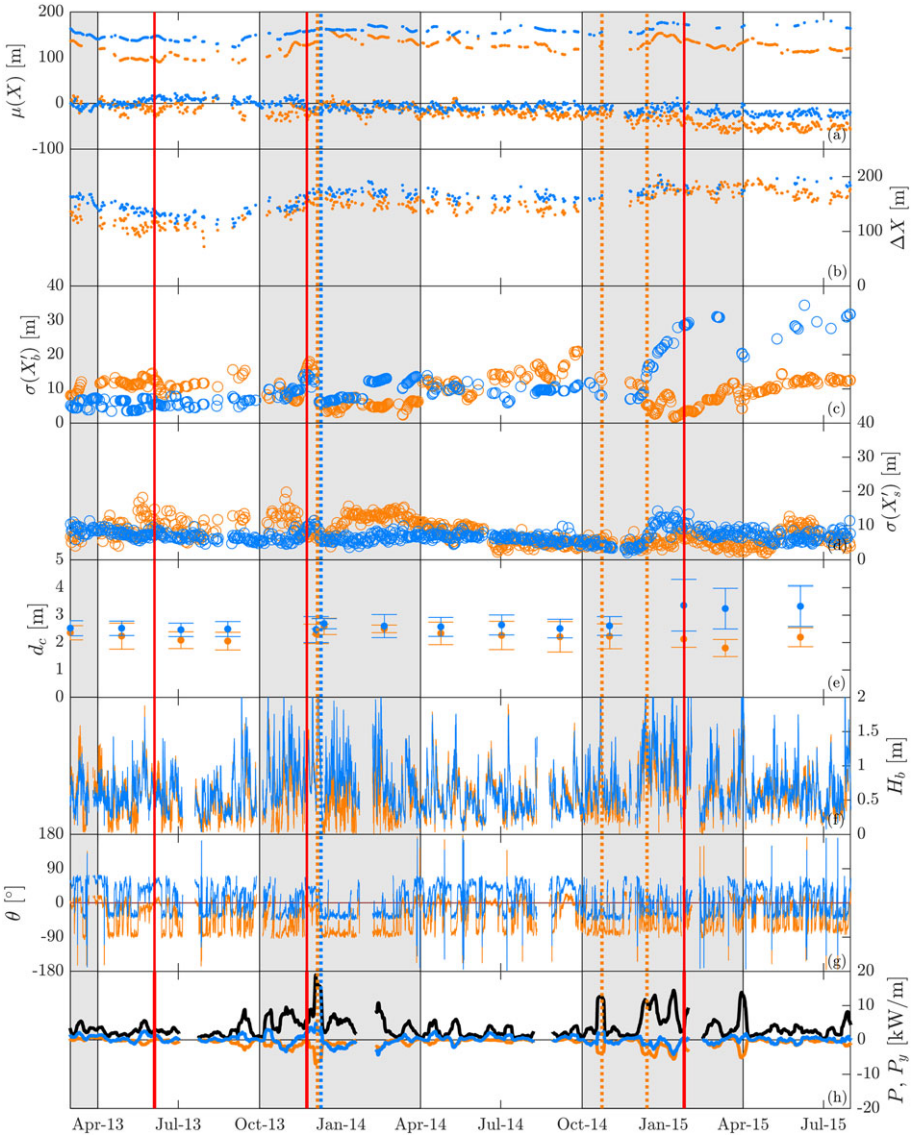


**Figure 8.** Temporal variability of (a) mean position $\mu(X)$ of the sandbar and MLW line (−0.68 m MSL) with zero $\mu(X)$ as the position of the MLW line in March 2013, (b) distance $\Delta\mu(X)$ between the sandbar and MLW (−0.68 m MSL), standard deviation in detrended (c) sandbar position $\sigma(X_b')$ and (d) MLW position $\sigma(X_s')$, (e) water depth above the sandbar crest $d_c$, (f) breaker height $H_b$, (g) wave angle $\theta$, and (h) the 8-day averaged wave power $P$ (black) and alongshore wave power $P_y$ at the northern (orange) and the western (blue) side. High values of $\sigma(X_b')$ and $\sigma(X_s')$ represent pronounced 3D patterning, whereas low values indicate a 2D barline and shoreline. The error bars in (e) indicate the standard deviation in $d_c$ within each box; large error bars reflect a high alongshore variability in $d_c$. The grey shading indicates the winter months, the vertical dashed lines the dates corresponding to sandbar straightening, and the vertical red lines the dates of the example plan view images of Figure 1. [Colour figure can be viewed at wileyonlinelibrary.com]

tively, seem to converge towards the pre-nourishment value of 42° from the north. The linear fit has a coefficient of determination $R^2$ of 0.82 at the northern side and 0.95 at the western side initially (July 2011); $R^2$ at the northern side increased rapidly beyond 0.95 in 6 months (July–December 2011). Figure 5c shows that the shore-normal, $\Phi_n$, changed from 366° to 332° over the northern side and from 275° to 295° over the western side, converging towards the pre-nourishment orientation of 312°. Note that the increase in $\Phi_n$ reduced at the western side from winter 2013–2014 onwards, while it continued to decrease at the northern side. The different rates of change of the −1 m contour at the northern and western side were also observed in the asymmetry of the plan shape, visualized in Figure 5d. Asymmetry was computed as $x^3/(x^2)^{1.5}$, where $x$ was the imaginary part of the Hilbert transform on the −1 m contour. Here, a negative asymmetry denotes a northward-pitching −1 m contour, whereas a positive asymmetry indicates that the −1 m contour pitches to the south. Thus the increase in asymmetry magnitude from −0.45 towards −0.3 from summer 2011 to summer 2014 reflects a change in planshape from northward pitching towards symmetrical. The largest changes were observed in autumn and winter (October–March), while the asymmetry hardly changed in spring and summer (March–October).

The Sand Engine was constructed with a convex, steep cross-shore profile, as shown in Figure 6. At both sides of the Sand Engine, the profile became concave within 6 months, due to fast erosion in the upper part of the profile ($z_b > -1$ m MSL). As a result, the subaqueous profile slope decreased. Figure 7 shows the temporal variation in profile slope, computed as the gradient of a linear fit through the alongshore-averaged cross-shore profile, at the northern and western side. In the first 6 months, the overall, subaqueous profile slope (between −1 m MSL and −8 m MSL) rapidly decreased, from 1:36 (0.028) to 1:50 (0.020) (Figure 7a) with fast erosion in the upper part of the profile (Figure 6). Thereafter, the slope continued to decrease, and started to converge to a cross-shore slope of 1:75 (0.013), which is slightly steeper

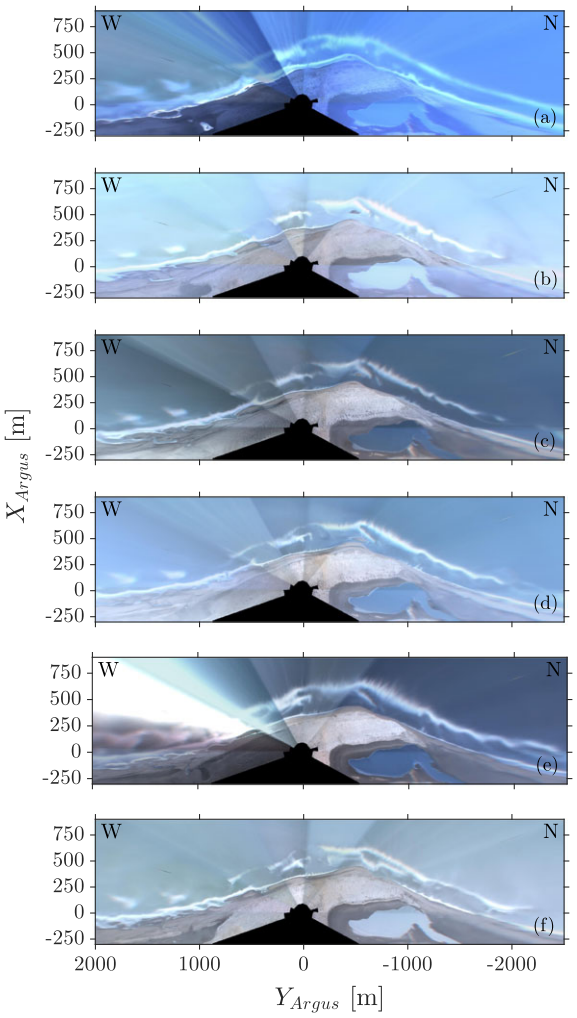


**Figure 9.** Argus 10 min averaged planviews from (a) 14 January 2015, (b) 10 February 2015, (c) 22 February 2015, (d) 5 March 2015, (e) 27 March 2015, and (f) 3 April 2015, showing how 3D patterns developed in the sandbar at the northern side. [Colour figure can be viewed at wileyonlinelibrary.com]

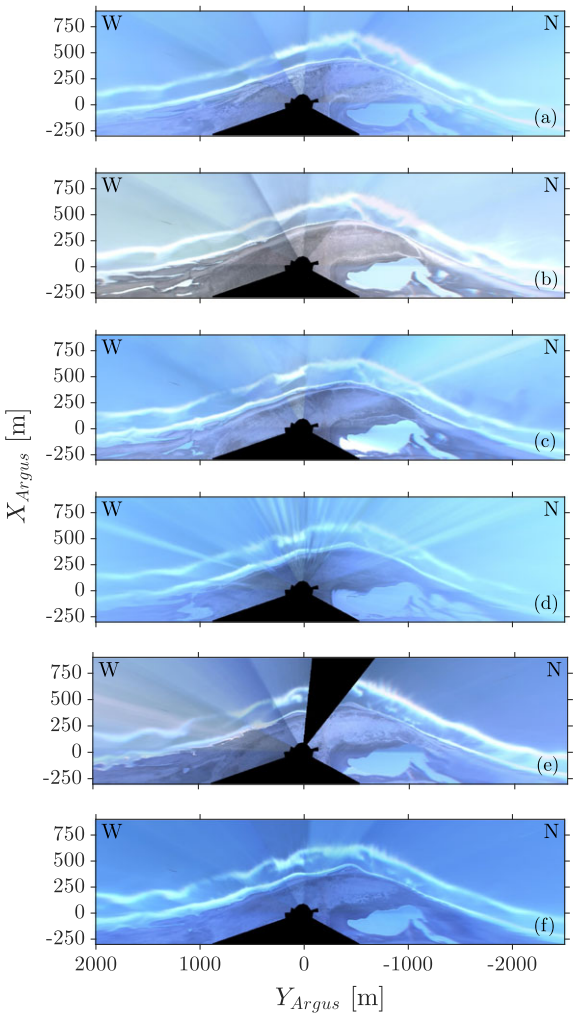


**Figure 10.** Argus 10 min averaged planviews from (a) 3 December 2014, (b) 9 December 2014, (c) 13 December 2014, (d) 19 December 2014, (e) 29 December 2014, and (f) 2 January 2015, showing how 3D patterns developed in the sandbar at the western side. [Colour figure can be viewed at wileyonlinelibrary.com]

than the pre-nourishment slope of 1:100 (0.010). The error bars, showing the standard deviation of the profile slope over both sides, indicate that the slope tended to become alongshore uniform with time. No significant difference was found between the profile response at the northern and western side. Similar to the slope of the overall profile, the intertidal slope showed an initial, rapid decrease to 1:49 (0.020) at the northern side and 1:56 (0.018) at the western side (Figure 7b). Thereafter, the slope became on average (January 2012 to September 2015) steeper: 1:32 (0.034) at the northern side, but milder, 1:62 (0.016) at the western side. The intertidal profile, probably influenced by the subtidal sandbars, showed substantial alongshore variations in slope. Moreover, the northern side showed a seasonal fluctuation with a steeper profile of up to 1:19 (0.053) in early spring (April) and a milder profile of up to 1:58 (0.017) in late autumn (December). The profile became milder with the build-up of a low-tide terrace (Figure 6a) during calm conditions, but also with erosion of the upper part of the beach due to overwash of the spit during storms. With ongoing storm conditions the low-tide terrace moved slightly offshore to larger depths, resulting in a steepening of the intertidal profile. In more detail, the temporal evolution of the low-tide terrace at the northern side and the classically Gaussian-shaped sandbar at the western side can be seen in Figure 6. Besides the difference in bar shape, note the differences in bar crest depth, 1.5 m versus 3 m, and cross-shore bar position, $x = 300$ m versus $x = 450$ m, between the northern and western side, respectively.

## Sandbar and shoreline behaviour

### Alongshore-uniform (2D) behaviour

Figure 8a shows that the sandbar was consistently located 125 m and 155 m from the initial MLW line at the northern and western side, respectively. Within 2.4 years, no net onshore or offshore migration can be observed, but $\mu(X_b)$ varied seasonally with offshore migration in winter and onshore migration in summer. In more detail, the sandbar started to migrate offshore with the first storm in autumn (September 2013 and October 2014; Figure 8f) and continued to do so until December/January, by up to 60 m at the northern side, and 35 m at the western side. Thereafter, $\mu(X_b)$ was either stable or decreased slowly during the summer months with low wave power. The observed offshore bar migration with winter storm waves and onshore bar migration with less-energetic summer waves is consistent with 2D bar migration elsewhere along the Dutch coast (Van Rijn *et al.*, 2003; Ruessink *et al.*, 2009; Pape *et al.*, 2010). Minor fluctuations in $\mu(X_b)$ can be observed throughout the year, especially at the northern side, but a clear response to every individual storm (e.g. Figure 8f) is not discernible, possibly because of a rather large volume

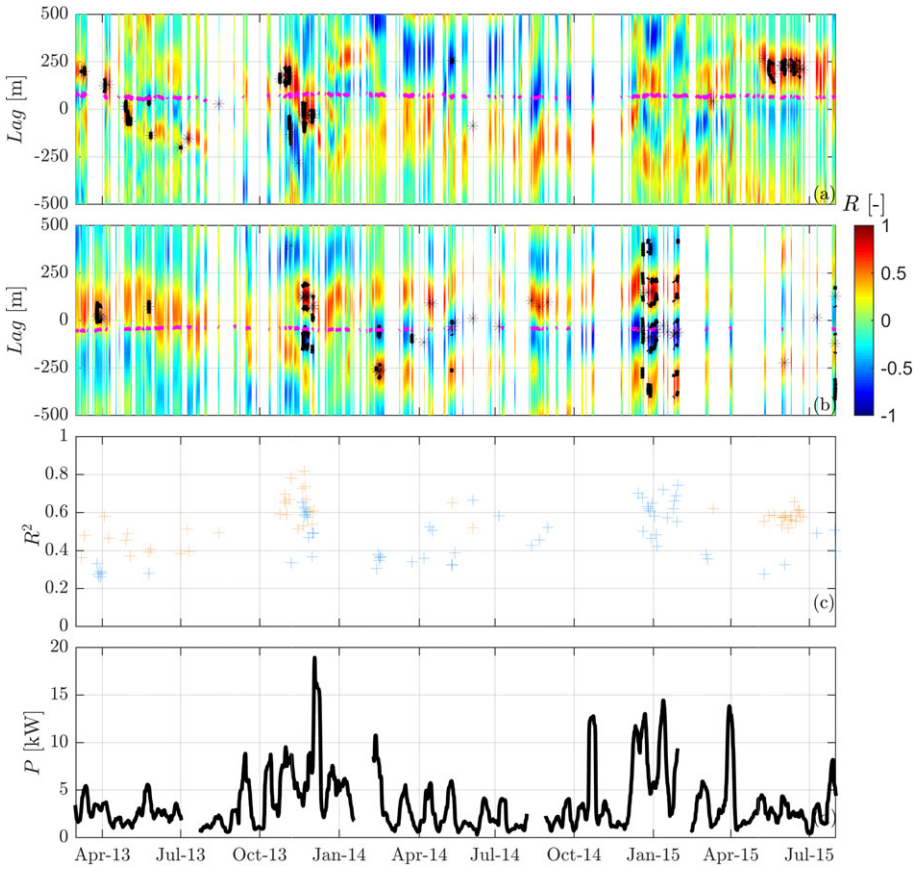


**Figure 11.** Lagged cross-correlation between the perturbations in the sandbar $X_b'$ and the MLW line $X_s'$ at the (a) northern side and at the (b) western side. Warm values indicate positive cross-correlation implying in-phase coupling, whereas cold colours represent negative coupling that can be interpreted as out-of-phase coupling. The black contours indicate the 98% significance level. The magenta lines in (a) and (b) show the zero lag that is corrected for the coastline orientation and the distance between the barline and shoreline at both sides. The squared correlation coefficient $R^2$ is plotted in (c) when significant at the 98% confidence level. For reference, the 8-day averaged wave power $P$ is shown in (d). [Colour figure can be viewed at wileyonlinelibrary.com]

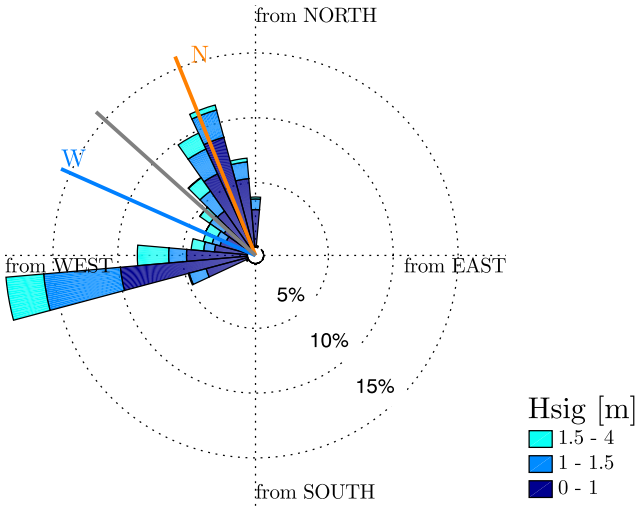


**Figure 12.** Wave conditions at 10 m water depth during the study period (March 2013 to July 2015). The radial lines indicate the shore-normal before construction of the Sand Engine (grey), and time-averaged over the study period for the northern side (orange) and the western side (blue). [Colour figure can be viewed at wileyonlinelibrary.com]

of sand constituting the bar compared to sites where a clear storm response was observed (Gallagher *et al.*, 1998; Ruessink *et al.*, 2009).

The seasonal migrational behaviour of the sandbars on both sides is also reflected in the water depth above the bar, $d_c$, computed from the *in situ* surveys (Figure 8e). Although the bar was located, on average, in shallower water at the northern side than at the western side, $d_c$ of 2 m MSL versus 2.5 m MSL, both sides had larger $d_c$ in winter, smaller $d_c$ in summer and up to 1 m inter-seasonal variability.

Figure 8b shows that the distance between the sandbar and MLW line, $\Delta\mu(X)$, increased from 130 m at the northern side and 160 m at the western side in March 2013 to 190 m and 180 m in March 2015, respectively. The increase can be attributed to the net retreat in $\mu(X_s)$ during the study period (Figure 8a). In more detail, the retreat in $\mu(X_s)$ slowed down at the northern side and even halted at the western side, under low wave power between March and November 2014 (Figure 8f). During the following low-energetic spring and summer (from March 2015 onwards), $\mu(X_s)$ was again rather stable. A rapid retreat was observed in November 2013 and February 2015. Before April 2013, no clear trends in $\mu(X_s)$ and accordingly $\Delta\mu(X)$ were observed (*in situ* data, not shown), because the dynamics of the MLW line were dominated by spit formation at the northern side and accumulation in the intertidal and subtidal zone at the western end, as described in the previous subsection ('Large-scale evolution') (Figures 5 and 6).

### Alongshore-variable (3D) behaviour

During the study period, 3D patterns developed regularly in the sandbar at both the northern and the western side, as represented by the increase in $\sigma(X_b')$ (measure for the horizontal amplitude of 3D patterns; Figure 8c) and the increase in the standard deviation of bar crest depth, $\sigma(d_c)$ (measure for the vertical amplitude of 3D patterns; error bars in Figure 8e).

Typically, $\sigma(X_b')$ increased up to $\sim$ 20 m (with the exception of $\sigma(X_b') = 30$ m at the western side). The temporal variability in $\sigma(X_b')$ and $\sigma(d_c)$ indicates that 3D behaviour at the northern and western sides differed substantially. For example, $\sigma(X_b')$ was up to 15 m at the northern side between April and October 2013 and decreased halfway November 2013, while at the western side $\sigma(X_b')$ was only 9 m and increased to 12 m in the second half of November 2013. Figure 8 shows that $\sigma(d_c)$ varied with $\sigma(X_b')$, i.e. the sandbars possessed an alongshore variability in both position and water depth. Note that the sandbar at the western side was highly 3D ($\sigma(X_b')$ of 30 m and $\sigma(d_c)$ of 1 m) in January 2015. Generally, 3D patterns formed gradually at the northern side within several months in spring and summer when wave power was low (Figure 8f), and were partially or fully smoothed out (known as bar straightening) within a few days with high wave power in autumn (e.g. December 2013, October 2014, December 2014). Contrastingly, 3D patterns developed within days–weeks at the western side under a series of moderate storms in autumn were hardly affected by the low-energetic spring and summer months, and were erased only once (synchronously timed with the northern side, under high wave power in December 2013). Similar to the 2D behaviour, the 3D behaviour also seems to be driven by a series of storms rather than every single storm event.

Video images further illustrate how the 3D patterns developed differently at each side. Figure 9 shows that the typical gradual increase in $\sigma(X_b')$ at the northern side can be explained by the merging of small-scale ($\sim$ 200 m) patterns that formed under calm conditions into larger-scale ($\sim$ 400 m) undulations under moderate conditions, as observed earlier by Van Enckevort *et al.* (2004). Figure 10 shows the formation of large-scale (400–500 m) undulations in several days of moderate wave power, typical for the western side. Wavelengths at both sides were smaller than observed further to the north along the Holland coast ($\sim$ 1000 m, Van Enckevort and Ruessink, 2003). Wavelengths were estimated through autocorrelation of the barlines. Although correlations were mostly not statistically significant for our dataset, they give an indication of the dominant wavelength, as found by Ruessink *et al.* (2007), who showed that wavelengths from autocorrelation, insignificant due to varying length scales along the barline, resembled the dominant lengths found with wavelet analysis. Figure 4 further illustrates that the wavelengths of 3D patterns were generally larger at the western side than at the northern side.

3D patterns in MLW position were generally less pronounced and fluctuated less in time than 3D patterns in sandbar position (Figure 8c, d). Despite this, a few rapid increases in $\sigma(X_s')$ were observed of 6–11 m in typically 20 days. At the western side, a growth in $\sigma(X_s')$ was accompanied by a growth in $\sigma(X_b')$ (December 2013, December 2014). This correspondence was less clear at the northern side. Here, undulations could persist for months, reflected by the high, stable signal in $\sigma(X_b')$ (e.g. January–March 2014). Decay of alongshore variability in the MLW line was either abrupt (December 2013) or gradual (March–June 2014, January–May 2015). Similar to the sandbar, the timing of growth and decay of 3D patterns in the MLW line differed between the northern and western side (e.g. December 2014, January 2015).

### Coupling

Figure 11 shows that morphological coupling between sandbar and shoreline was, at times, significant: 6.7% of all observations at the northern side and 7.8% at the western side, with a mean correlation coefficient $R^2$ of 0.57 and 0.48, respectively. For 49% of the observations at the northern side and 56% at the western side no cross-correlation could be computed, because at least one of the breaker lines was missing. Generally, sandbar and shoreline were uncorrelated at zero lag. However, a significant, positive correlation (in-phase coupling) was found at the northern side for 6.0% of the observations with a bimodal distributed lag, centred at $m = -30$ m and $m = 210$ m. At the western side, 4.6% of the observations had a positive correlation (in-phase coupling) with a bimodal lag centred at $m = -270$ m and $m = 90$ m, and 3.2% had a significant, negative correlation (out-of-phase coupling) with a lag of $m = -90$ m. Given that the coordinate system was not aligned with the coastline, a positive correlation with either a small negative lag (or large positive lag) at the northern side or a small positive lag (or large negative lag) at the western side represents an unshifted out-of-phase coupling for the local coastline orientation. Similarly, negative correlations can be interpreted as a locally unshifted out-of-phase coupling, for small positive lag at the northern side and small negative lag at the western side. Note that the lag of significant correlation decreased with a smaller distance between sandbar and shoreline and with smaller plan shape curvature. To summarize, the modal lags computed here seem to apply to an unshifted out-of-phase coupled sandbar and shoreline, considering the local coastline orientation. The 'zero-lag' for the local coastline orientation (magenta line in Figure 11), estimated from $\Delta\mu(X)$ and $\Phi$, confirms that the sandbar and shoreline were generally coupled out-of-phase (e.g. see western side in Figure 1c) as observed elsewhere (Thornton *et al.*, 2007; Van de Lageweg *et al.*, 2013; Castelle *et al.*, 2015). A minor temporal variation exists in the lag of significant coupling, of up to $\sim$80 m (Figure 11a, b, e.g. January 2015), but it is small compared to the wavelength of the 3D patterns (200–500 m). Coupling patterns were strongest at the western side from December 2014 until July 2015, when also 3D patterns were most pronounced. Sandbar and shoreline did not couple and decouple synchronously at the two sides (e.g. December 2014; see Figure 11a–c).

## Discussion

In this section, we analyse the wave conditions to determine what forcing parameters governed the observed sandbar behaviour and drove the distinct differences in morphology at the northern and western side of the curved coast. In particular, we focus on breaker height and wave angle.

### Breaker height

The northern and western sides differed in their typical surfzone morphology, apparent from the bar shape, the distance between sandbar and shoreline, and the wavelength of 3D patterns. These morphological characteristics are probably related to each other (e.g. Calvete *et al.*, 2005) and are thus not statistically independent. The low-tide terrace at the northern side, typically closely located to or connected to the beach with relatively small ($\sim$ 200 m) length scales of 3D patterns, suggests an exposure to moderate energetic wave conditions only (Wright and Short, 1984). In contrast, the pronounced Gaussian-shaped sandbar at the western side, which was typically positioned $\sim$ 200 m offshore at $\sim$ 2.7 m water depth, having 3D patterns with length scales of 400–500 m, is indicative of more energetic conditions.

During our 2.4-year study period (Figure 12), waves came predominantly from the north-northwest and the west (bimodal climate), consistent with the above-mentioned long-term wave climate characteristics. Figure 12 shows that

wave heights were of equal magnitude for both directional modes, given that wave refraction effects were neglected. Wave height, however, decreases with refraction, which at the Sand Engine is especially important for highly oblique westerly waves approaching the northern side. To illustrate that the northern side was exposed to less energetic conditions than the western side, including refraction effects, the breaker wave height $H_b$ was computed over the 2.4-year study period. Both the 50th percentile (median) as well as the 90th percentile of $H_b$ were lower at the northern side compared to the western side: 0.53 m versus 0.59 m and 1.0 m versus 1.2 m, respectively. Figure 8f shows also that $H_b$, varying with the local wave angle (Figure 8g), was generally higher at the western side. On the whole, our results indicate that alongshore variability in sandbar characteristics were related to alongshore variability in wave height imposed by the curved shape of the Sand Engine.

## Wave angle

The sandbars at the northern and western sides responded differently to the same offshore time-varying wave forcing (Figure 8). Differences in 2D behaviour concerned the cross-shore migration rates of the sandbars (e.g. December 2014, Figure 8) and the shortest timescales over which the bars migrated (seasonal versus intra-seasonal). Differences in 3D behaviour mainly concerned the wavelength of the 3D patterns, and timing in their development, even resulting in opposite behaviour at the northern and western side (e.g. December 2014: growth versus decay of 3D patterns, Figure 8). Similarly, a timing difference in morphological coupling was observed between both sides. The timing differences in 3D sandbar response and morphological coupling between both sides may be explained by the local wave angle. Figure 12 shows that most waves, as a result of the coastline curvature, approached either shore-normally or very obliquely ($\sim 80°$) at the northern side, while predominantly obliquely ($\sim 36$ and $\sim 44°$) at the western side. For reference, waves entered predominantly obliquely ($\sim 54$ and $\sim 26°$) before construction of the Sand Engine. At the northern side, the growth of 3D patterns in the sandbar (Figure 8c) coincided with prolonged periods of near-zero wave incidence and moderate wave height ($H_b = 1.0 - 1.5$ m, e.g. March 2013, April–October 2014, Figure 8f, g), consistent with Wright and Short (1984), Calvete *et al.* (2005), Drønen and Deigaard (2007) and Splinter *et al.* (2011), all of whom showed that 3D patterns in sandbars form preferably under low-energetic, shore-normal waves. At the western side, contrastingly, 3D patterns formed rapidly with the passage of several storms, characterized by a shifting wave angle $\theta_W = -30$ to $40°$ and peaks in $H_b$ of 1.5–2 m. Such behaviour, with increasing 3D patterning in the storm season, is similar to the 3D behaviour observed at Vlugtenburg, a few kilometres south of our study site (De Schipper *et al.*, 2013). We find that sandbar straightening events at both the northern (December 2013, October 2014 and December 2014) and western side (December 2013) coincided with peaks of 4–6 kW m$^{-1}$ in the 8-day averaged longshore wave power $P_y$, suggesting that oblique waves of substantial height over 1–2 days, presumably driving a strong longshore current, were needed to erase the 3D patterns. The infrequent bar straightening at the western side may be explained by the generally small peaks in $P_y$. Similarly, we expect that the highly 3D bar in January 2015 would require higher $P_y$ to straighten. The asynchronous response for the northern and western side, e.g. in December 2014 with bar straightening at the northern side versus a growth of 3D patterns at the western side, may be related to local differences in $P_y$, which, accordingly, is the consequence of the coastline orientation. Similarly, timing differences in coupling between sandbar and shoreline patterns, related to timing differences in 3D patterning, may also depend on the wave angle. Although, generally, cross-correlations were significant when the 3D patterns in the sandbar were pronounced (Figure 11; April–August 2013, November 2013 and May–June 2015 for the northern side; November 2013 and December 2014 to July 2015 for the western side), no significant cross-correlation was found at the northern side in summer 2014, when the bar was 3D. Possibly, the absence of a distinct bar trough or the distance between sandbar and shoreline (Figure 6; Wright and Short, 1984) may explain the lack of coupling due to a weakened cell circulation. Castelle *et al.* (2010) showed for a double sandbar system how alongshore differences in wave breaking over a 3D outer bar generate such horizontal circulation cells that drive bed-level changes shoreward of the bar, creating a coupled patterning in the inner bar.

Our observation that the wave angle determines to a large extent the 3D behaviour at the curved Sand Engine is in line with previous studies along straight coasts. For example, Thornton *et al.* (2007) and Price and Ruessink (2011) found that 3D patterns developed under near-normal waves, and Price and Ruessink (2011, 2013), Garnier *et al.* (2013) and Contardo and Symonds (2015) found that bar straightening and decoupling related to oblique waves. According to model predictions (Thiébot *et al.*, 2012; Ashton *et al.*, 2001), patterns in the shoreline and adjacent depth contours can also be related to highly oblique angles. Thiébot *et al.* (2012) showed that down-current oblique bars developed with an alongshore spacing of $\sim 100$ m along the inner bar of a double bar system for $21 < \theta < 31°$ at the outer bar crest. We are not aware of any field evidence on such pattern formation, but bar geometries seem similar to the erosional Transverse Bar and Rip state observed along the Gold Coast, Australia (Price and Ruessink, 2011) or the skewed Transverse Bar and Rip state along the Aquitaine coast, France (Castelle *et al.*, 2007). Note, however, that their formation mechanism is different, as they are more likely to be reoriented pre-existing morphological patterns. Thiébot *et al.* (2012), furthermore, demonstrated that up-current elongated features developed when increasing the wave angle beyond 31° at the outer bar crest, with alongshore wavelengths of $\sim 70$ m extending hundreds of metres offshore. Those so-called finger bars have been regularly observed in the field, i.e. Duck, USA (Konicki and Holman, 2000), Noordwijk, Netherlands (Ribas and Kroon, 2007) and the Gold Coast, Australia (Ribas *et al.*, 2014). At the Sand Engine, both oblique bars and finger bars have been observed occasionally (Figure 13), especially at the northern side, where the westerly mode was highly oblique (Figure 12). Patterns simulated by Ashton *et al.* (2001), also referred to as shoreline sand waves, are related to gradients in the alongshore sediment transport that destabilize the shoreline and adjacent bathymetric contours (Ashton and Murray, 2006). Ashton and Giosan (2011) showed that shoreline patterns developed along one of the two flanks of an arcuate-shaped river delta under highly oblique waves. Although patterns seem similar to the shoreline undulations at our site, length and timescales of these shoreline sand waves are typically larger, 1–10 km versus 200–500 m and $O(100)$ years versus several months. Moreover, Arriaga *et al.* (2017) showed that the Sand Engine is just below the instability threshold and thus, in the long term, will not grow by itself or trigger instabilities at the adjacent straight coastline.

Although high-angle waves may have played a role at the Sand Engine in generating 3D patterns, given the occasional presence of oblique transverse bars and finger bars, we attribute the variability in $\sigma(X')$, representing the patterning

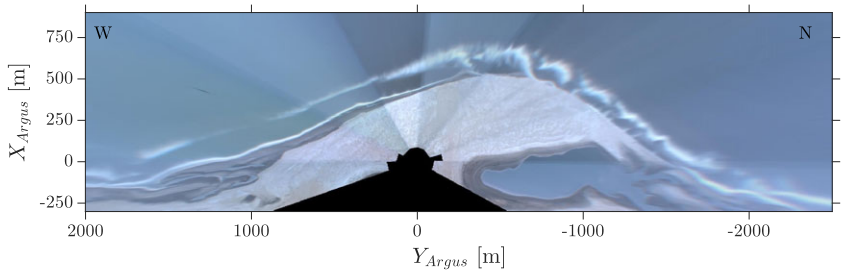


**Figure 13.** Argus time exposure image from 4 April 2013, showing the presence of finger bars (white elongated features attached to the shoreline and pointing offshore) at $-1300 < Y_{\text{Argus}} < -1000$ m and oblique transverse bars at $-700 < Y_{\text{Argus}} < -300$ m. [Colour figure can be viewed at wileyonlinelibrary.com]

in sandbar and shoreline, largely to low-angle waves. First, oblique bars and finger bars were relatively rarely observed and thus they hardly contributed to $\sigma(X')$. Oblique bars hardly affected the barline, but only the shoreline (see Figure 13). No variability due to finger bars is included in $\sigma(X')$, since extracted breaker lines were filtered for length scales shorter than 75 m. Second, shoreline patterns in our observations arose in particular when sandbar patterns were already pronounced, and thus seem, in contrast to shoreline sand waves, to be related to surf zone circulation with the sandbar acting as a morphological template. This is confirmed by Figure 11, showing significant coupling between sandbar and shoreline patterns when the sandbar was 3D. Therefore, the mechanism on pattern formation along a curved coast, as proposed by Ashton and Giosan (2011), is not applicable here to the variability in $\sigma(X')$.

Although our dataset covers 2.5 years only, which is relatively short with respect to the Sand Engine's expected lifetime of several decades (Arriaga *et al.*, 2017), the duration is of sufficient length to raise the hypothesis that the wave height and angle are key to the observed alongshore differences in bar behaviour at daily to seasonal timescales. We expect that differences in bar behaviour between both sides may decrease in time, given the decrease in curvature under foreseen ongoing diffusion (Arriaga *et al.*, 2017) with orientations of both sides becoming more similar. Herein, the sandbars may respond differently than expected given the previous history of both sides. For example, Tiessen *et al.* (2011) showed that differences in pre-existing bedforms may affect the wavelength of subsequently evolving crescentic patterns. Also, the northern and western sides may start to influence each other in time, and thus being no longer independent in their morphological evolution. Our work implies that bar behaviour along curved coasts, e.g. shoreline sand waves, cuspate forelands or embayed beaches, may show substantial alongshore variation wherein local wave forcing, i.e. wave height or wave angle, is important. To assess more closely how wave angle, wave height or coastline curvature control bar behaviour along a curved coast, we will use a morphodynamic model in a future study. This will allow us to systematically test and analyse the individual effects of wave angle, wave height and curvature. In addition, by varying the coastline curvature, we can mimic the non-stationarity of curved coasts (e.g. the diffusion of the Sand Engine shown here). Also, the simulations will reveal the sediment transport patterns and underlying flow field that drive the distinct morphological changes.

## Conclusion

Along the man-made curved coast of the Sand Engine, both similarities and differences in sandbar and shoreline behaviour were observed. Similarities in 2D bar behaviour between the northern and western side include the onshore and offshore bar migration coinciding with the seasonally varying wave power, balancing to nearly zero migration on inter-annual timescales. Also, the distance between sandbar and shoreline increased in time at both sides, given the ongoing shoreline retreat related to the diffusion of the Sand Engine, and the rather stable position of the sandbars on inter-annual timescales. The differences in bar geometry between both sides (3D length scales, distance from the shoreline, bar crest depth and bar shape) suggest that the northern side was governed by lower energetic conditions than the western side, which was confirmed by $H_b$ (1.0 m versus 1.2 m for the 90th percentile), locally different due to longshore differences in wave refraction.

Three-dimensional behaviour, i.e. growth, straightening and coupling of 3D patterns in the sandbar and shoreline, differed between both sides, especially in timing. Whereas 3D patterns formed gradually in summer under prolonged periods of north-northwestern, moderate, shore-normal waves ($\theta_N = 0°$, $H_b = 1 - 1.5$ m) at the northern side, they developed rapidly (days–weeks) under a series of southwestern–western autumn storms ($\theta_W = -30$ to $40°$, $H_b = 1.5 - 2$ m) at the western side. The 3D patterns decayed under highly oblique waves when the 8-day averaged longshore wave power peaked ($P_y > 4$ kW m$^{-1}$). This happened more often on the northern than the western side. A coupled sandbar and shoreline were mostly found in periods when 3D patterns were pronounced. Our findings on 3D behaviour suggest that the local difference in wave angle, imposed by the curved coast, explains the observed timing differences in 3D behaviour.

Although further study is needed to unravel the exact physical processes driving the intriguing differences in sandbar and shoreline behaviour along a curved coast, we conclude that such a coast imposes locally different wave conditions, in terms of wave height and wave angle, that, in turn, lead to substantial alongshore differences in subtidal sandbar dynamics.

## Appendix A: Accuracy of sandbar and shoreline positions

In our study we relied on the variability in the position and planshape of breaker lines in Argus imagery to quantify sandbar and shoreline behaviour. However, these breaker lines are only an indirect measure of the underlying sandbars. How accurate they approximate the position of the sandbar crest and the shoreline is unknown for our site. In this Appendix we assess the accuracy of the breaker line method by comparison with *in situ* measurements.

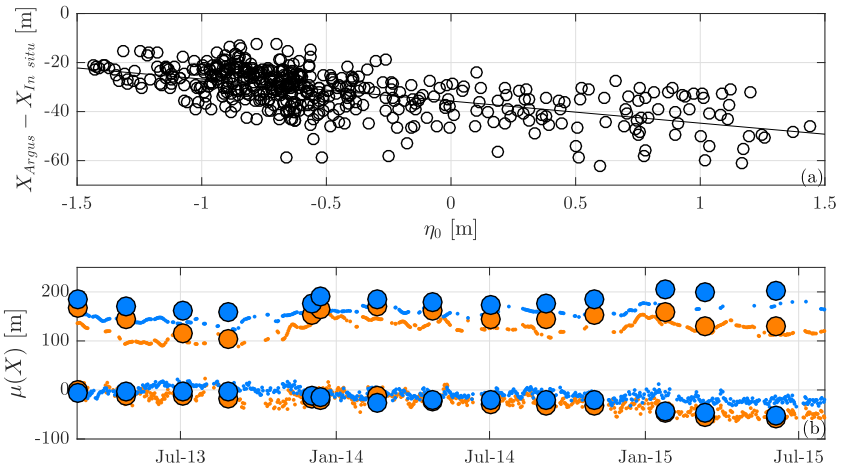


**Figure A1.** Difference in mean cross-shore sandbar position (a), defined as $\Delta\mu(X) = \mu(X_{\text{Argus}}) - \mu(X_{in\ situ})$, during 31 days as a function of the offshore measured water level $\eta_0$. Mean position $\mu(X)$ (b) of the sandbar ($100 < \mu(X) < 200$ m) and MLW line ($-100 < \mu(X) < 0$ m) extracted from the video images (small dots) and compared with *in situ* measurements (large dots). Zero $\mu(X)$ represents the MLW line in March 2013, whereas orange indicates the northern side and blue the western side. [Colour figure can be viewed at wileyonlinelibrary.com]

## Barline

Firstly, we determined the variability in cross-shore position of the barline from the *in situ* measured bar crest, under tide-induced water-level fluctuations. We used a 31-day dataset (March 2013) of 799 Argus images, sampled every 30 min during daylight, wherein 483 barlines were extracted at the western side and actual bar migration was limited (observed in *in situ* measurements). Bar crests were extracted from *in situ* measurements as the maximum perturbation in each shore-normal profile. With this technique, based on the method in Grunnet and Ruessink (2005), we can also evaluate characteristics of the platform-shaped sandbars at the northern side of the Sand Engine. Perturbation profiles were generated by subtracting a featureless profile, created for each profile using a loess filter (Plant *et al.*, 2002) with a smoothing length $Lx = 125$ m, from the barred profile that was filtered for small-scale noise ($Lx = 50$ m). From all perturbations with a minimum height of 0.4 m and separated by at least 20 m, the most offshore perturbation (for $-5.5$ m $< z < -1$ m) was selected as the bar crest. Bar crest positions were checked visually and were extracted manually when necessary. Then, the bias in mean cross-shore sandbar position was computed, $\Delta\mu(X_b) = \mu(X_{b,\text{Argus}}) - \mu(X_{b,in\ situ})$. For the 31-day study period, $\mu(X_{b,in\ situ})$ (two surveys) was linearly interpolated over 799 time steps corresponding to the image sampling times. Figure A1a shows a clear tidal dependency for the mean cross-shore barline position, consistent with Van Enckevort and Ruessink (2001). The barline shifted 9 m offshore during a 1 m decline in water level. This tide-induced variability in barline position can be removed by considering a selection of images during a single tidal level, following Van Enckevort and Ruessink (2001) and Ruessink *et al.* (2002). Here, we chose for low-tide images during which breaking is most pronounced, leaving us a dataset of 778 images over the total 2.4-year period. An additional variability in barline position due to a water-level fluctuation caused by the spring–neap cycle was smoothed by a Hanning filter with a window of 14.77 days (similar to (Ruessink *et al.*, 2002)). No correction was performed for a potential wave-induced variability on $X_b$ (Ribas *et al.*, 2010; Pape *et al.*, 2010), because local wave height and angle were not available. As a result, the remaining variability in $X_b$ on daily timescales may be wave induced, whereas changes in $X_b$ that persist for weeks to months are assumed to reflect behavioural dynamics of the sandbar itself.

**Table AI.** Bias, defined as $\Delta\mu(X) = \mu(X_{\text{Argus}}) - \mu(X_{in\ situ})$, and root mean square error, $\varepsilon_{\text{RMS}}$, in mean position of the sandbar $X_b$ and the shoreline $X_s$ derived from Argus video and *in situ* measurements at the Sand Engine

| | North side | West side |
|---|---|---|
| $\Delta\mu(X_b)$ | −21 m | −25 m |
| $\varepsilon_{\text{RMS}}$ $X_b$ | 26 m | 39 m |
| $\Delta\mu(X_s)$ | 4 m | 13 m |
| $\varepsilon_{\text{RMS}}$ $X_s$ | 10 m | 18 m |

Secondly, we determined the remaining bias, $\Delta\mu(X_b)$, and the root mean square error, $\varepsilon_{\text{RMS}}$, after removing the tide-induced variability in cross-shore barline position within the 2.4-year dataset. *In situ* bar crests were extracted from 14 surveys. We found that the barline was generally located shoreward (negative $\Delta\mu(X_b)$) of the measured bar crest at $O$(10 m) (Table AI; Figure A1b), in line with the findings of Van Enckevort and Ruessink (2001). Slightly higher $\Delta\mu(X_b)$ and $\varepsilon_{\text{RMS}}$ can be observed at the western side compared to the northern side, which can possibly be explained by different bar crest depth and bar shape at either side (see Van Enckevort and Ruessink, 2001; Ribas *et al.*, 2010). Similarly, the temporal variability in $\Delta\mu(X_b)$ (Figure A1b) may be explained by time variations in bar crest depth and bar shape.

To conclude, at our site the outer breaker line in video imagery approaches the sandbar crest position with an O(10 m) accuracy, when accounting for tide-induced variability, and thus, given the larger actual variability in sandbar position (see Figure A1b), we reason that we may safely use the breaker line method to quantify sandbar behaviour here.

## Shoreline

Prior to assessing the accuracy of the mean cross-shore position of the shoreline with *in situ* measurements, two methodological steps were needed to limit tide- and wave-induced shifting of the shoreline. Firstly, the water-level elevation was estimated corresponding to each extracted shoreline, using the correction model of Aarninkhof *et al.* (2003). Accordingly,

water-level elevation was computed for each extracted shoreline, $z_s$, as follows:

$$z_s = z_0 + \eta_s + 0.5 K_{osc} \eta_{osc}, \quad \text{(A1)}$$

with offshore water level $z_0$, wave-setup $\eta_s$, a constant empirical coefficient $K_{osc}$, and swash height $\eta_{osc}$. Model input terms were computed from measured tide and wave statistics (see *Image and field data*). For further details on the model we refer to Aarninkhof *et al.* (2003). Following Plant *et al.* (2007), $K_{osc}$ was adjusted from 1.2 (default) to −0.48, to optimize the fit for shorelines based on breaker lines instead of colour differences (hue, saturation, value) as in Aarninkhof *et al.* (2003). Secondly, shorelines were translated to the MLW line, at −0.68 m MSL, given the elevation and cross-shore position of each shoreline, and assuming an alongshore-uniform beach slope of 0.03. From the *in situ* measurements, the MLW line was simply extracted as the corresponding elevation contour. We found that the shoreline showed generally a small seaward offset (Table AI; Figure 7b). Shorelines at the western side had a slightly larger $\Delta\mu(X_s)$ and $\varepsilon_{RMS}$ compared to the northern side. Possibly, the offset of $X_s$ can be explained by deviations in the beach face slope from the assumed 0.03 (Figure 7b), as used in the model, or by uncertainty in the value of $K_{osc}$.

Altogether, given the ∼ 10 m accuracy of video-derived shorelines at our site, we may rely on the breaker line method to quantify and describe shoreline behaviour.

*Acknowledgements*— J.R. and B.G.R. were funded by the Dutch Technology Foundation STW, which is part of the Dutch Organisation for Scientific Research (NWO), and which is partly funded by the Ministry of Economic Affairs, under contract 12686 (Nature Coast: S1 Coastal Safety). T.D.P. was funded by the Dutch Organisation for Scientific Research (NWO), under contract 016.Veni.171.101. We acknowledge Deltares for the collection of the Argus imagery, and SHORE Monitoring & Research for the collection of the bathymetric data.

## References

Aagaard T, Kroon A. 2007. Mesoscale behaviour of longshore bars net onshore or net offshore migration. In *Proceedings of Coastal Sediments World Scientific,* Singapore; 2124—2136.

Aarninkhof SGJ, Turner IL, Dronkers TDT, Caljouw M, Nipius L. 2003. A video-based technique for mapping intertidal beach bathymetry. *Coastal Engineering* **49**: 275–289.

Arriaga J, Rutten J, Ribas F, Falqués A, Ruessink BG. 2017. Modeling the long-term diffusion and feeding capability of a mega-nourishment. *Coastal Engineering* **121**: 1–13.

Ashton AD, Giosan L. 2011. Wave-angle control of delta evolution. *Geophysical Research Letters* **38**: L13405. https://doi.org/10.1029/2011GL047630.

Ashton AD, Murray AB. 2006. High-angle wave instability and emergent shoreline shapes. 1. Modeling of sand waves, flying spits, and capes. *Journal of Geophysical Research* **111**: F04011. https://doi.org/10.1029/2005JF000422.

Ashton A, Murray AB, Arnault O. 2001. Formation of coastline features by large-scale instabilities induced by high-angle waves. *Nature* **414**: 296–300.

Backstrom JT, Jackson DWT, Cooper JAG, Malvárez GC. 2008. Storm-driven shoreface morphodynamics on a low-wave energy delta: the role of nearshore topography and shoreline orientation. *Journal of Coastal Research* **24**: 1379–1387.

Blossier B, Bryan KR, Daly CJ, Winter C. 2016. Nearshore sandbar rotation at single-barred embayed beaches. *Journal of Geophysical Research: Oceans* **121**: 2286–2313. https://doi.org/10.1002/2015JC011031.

Calvete D, Dodd N, Falqués A, van Leeuwen SM. 2005. Morphological development of rip channel systems: normal and near-normal wave incidence. *Journal of Geophysical Research C: Oceans* **110**: C10006. https://doi.org/10.1029/2004JC002803.

Castelle B, Bonneton P, Dupuis H, Sénéchal N. 2007. Double bar beach dynamics on the high-energy meso-macrotidal French Aquitanian Coast: a review. *Marine Geology* **245**: 141–159.

Castelle B, Ruessink BG, Bonneton P, Marieu V, Bruneau N, Price TD. 2010. Coupling mechanisms in double sandbar systems. Part 1. Patterns and physical explanation. *Earth Surface Processes and Landforms* **35**: 476–486.

Castelle B, Marieu V, Bujan S, Splinter KD, Robinet A, Sén'echal N, Ferreira S. 2015. Impact of the winter 2013–2014 series of severe Western Europe storms on a double-barred sandy coast: beach and dune erosion and megacusp embayments. *Geomorphology* **238**: 135–148.

Chong TY. 2014. *Assessment of beach states at the Sand Motor on the basis of alongshore variability in bathymetry data*. MSc thesis, TU Delft, Netherlands.

Contardo S, Symonds G. 2015. Sandbar straightening under wind–sea and swell forcing. *Marine Geology* **368**: 25–41.

Davidson-Arnott RGD, Van Heyningen AG. 2003. Migration and sedimentology of longshore sandwaves, Long Point, Lake Erie, Canada. *Sedimentology* **50**: 1123–1137.

De Schipper MA, De Vries S, Ranasinghe R, Reniers AJHM, Stive MJF. 2013. Alongshore topographic variability at a nourished beach. In *Proceedings of the 7th International Conference on Coastal Dynamics*, Bordeux University, Bordeux; 499–510.

De Schipper MA, De Vries S, Ruessink BG, De Zeeuw RC, Rutten J, Van Gelder-Maas C, Stive MJF. 2016. Initial spreading of a mega feeder nourishment: observations of the Sand Engine pilot project. *Coastal Engineering* **111**: 23–38.

Drønen N, Deigaard R. 2007. Quasi-three-dimensional modelling of the morphology of longshore bars. *Coastal Engineering* **54**: 197–215.

Elgar S, Gallagher EL, Guza RT. 2001. Nearshore sandbar migration. *Journal of Geophysical Research* **106**: 11623–11627.

Gallagher EL, Elgar S, Guza RT. 1998. Observations of sand bar evolution on a natural beach. *Journal of Geophysical Research* **103**: 3203–3215.

Gallop SL, Bryan KR, Coco G, Stephens SA. 2011. Storm-driven changes in rip channel patterns on an embayed beach. *Geomorphology* **127**: 179–188.

Garnier R, Falqués A, Calvete D, Thiébot J, Ribas F. 2013. A mechanism for sandbar straightening by oblique wave incidence. *Geophysical Research Letters* **40**: 2726–2730.

Garrett C, Toulany C. 1981. Variability of the flow through the Strait of Belle Isle. *Journal of Marine Research* **39**: 163–189.

Grunnet NM, Ruessink BG. 2005. Morphodynamic response of nearshore bars to a shoreface nourishment. *Coastal Engineering* **52**: 119–137.

Harley MD, Turner IL, Short AD. 2015. New insights into embayed beach rotation: the importance of wave exposure and cross-shore processes. *Journal of Geophysical Research: Earth Surface* **120**: 1470–1484.

Hoefel F, Elgar S. 2003. Wave-induced sediment transport and sandbar migration. *Science* **299**: 1885–1887.

Holland TK, Holman RA, Lippmann TC, Stanley J, Plant NG. 1997. Practical use of video imagery in nearshore oceanographic field studies. *IEEE Journal of Oceanic Engineering* **22**: 81–92.

Holman RA, Stanley J. 2007. The history and technical capabilities of Argus. *Coastal Engineering* **54**: 477–491.

Holman RA, Symonds G, Thornton EB, Ranasinghe R. 2006. Rip spacing and persistence on an embayed beach. *Journal of Geophysical Research: Oceans* **111**: C01006. https://doi.org/10.1029/2005JC002965.

Komar PD. 1976. *Beach Processes and Sedimentation*. Prentice Hall: New York.

Konicki KM, Holman RA. 2000. The statistics and kinematics of transverse sand bars on an open coast. *Marine Geology* **169**: 69–101.

Lippmann TC, Holman RA. 1989. Quantification of sand bar morphology: a video technique based on wave dissipation. *Journal of Geophysical Research* **94**: 995–1011.

Lippmann TC, Holman RA. 1990. The spatial and temporal variability of sand bar morphology. *Journal of Geophysical Research* **95**: 11575–11590.

McCarroll RJ, Brander RW, Turner IL, Van Leeuwen B. 2016. Shoreface storm morphodynamics and mega-rip evolution at an

embayed beach: Bondi Beach, NSW, Australia. *Continental Shelf Research* **116**: 74–88.

Ojeda E, Ruessink BG, Guillen J. 2008. Morphodynamic response of a two- barred beach to a shoreface nourishment. *Coastal Engineering* **55**: 1185–1196.

Ojeda E, Guillén J, Ribas F. 2011. Dynamics of single-barred embayed beaches. *Marine Geology* **280**: 76–90.

Pape L, Plant NG, Ruessink BG. 2010. On cross-shore migration and equilibrium states of nearshore sandbars. *Journal of Geophysical Research* **115**: F03008. https://doi.org/10.1029/2009JF001501.

Plant NG, Holland KT, Puleo JA. 2002. Analysis of the scale of errors in nearshore bathymetric data. *Marine Geology* **191**: 71–86.

Plant NG, Aarninkhof SGJ, Turner IL, Kingston KS. 2007. The performance of shoreline detection models applied to video imagery. *Journal of Coastal Research* **23**: 658–670.

Price TD, Ruessink BG. 2011. State dynamics of a double sandbar system. *Continental Shelf Research* **31**: 659–674.

Price TD, Ruessink BG. 2013. Observations and conceptual modelling of morphological coupling in a double sandbar system. *Earth Surface Processes and Landforms* **38**: 477–489.

Quartel S, Kroon A, Ruessink BG. 2008. Seasonal accretion and erosion patterns of a microtidal sandy beach. *Marine Geology* **250**: 19–33.

Ranasinghe R, McLoughlin R, Short A, Symonds G. 2004a. The Southern Oscillation Index, wave climate, and beach rotation. *Marine Geology* **204**: 273–287.

Ranasinghe R, Symonds G, Black K, Holman RA. 2004b. Morphodynamics of intermediate beaches: a video imaging and numerical modelling study. *Coastal Engineering* **51**: 629–655.

Ribas F, Kroon A. 2007. Characteristics and dynamics of surfzone transverse finger bars. *Journal of Geophysical Research* **112**. https://doi.org/0.1029/2006JF000685.

Ribas F, Ojeda E, Price T D, Guillén J. 2010. Assessing the suitability of video imaging for studying the dynamics of nearshore sandbars in tideless beaches. *IEEE Transactions on Geoscience and Remote Sensing* **48**: 2482–2497.

Ribas FA, De Swart HE, Doeschate A, Calvete D, Ruessink BG. 2014. Observations and modeling of surf zone transverse finger bars at the Gold Coast, Australia. *Ocean Dynamics* **64**: 1193–1207.

Ruessink BG, Bell PS, Van Enckevort IMJ, Aarninkhof SGJ. 2002. Nearshore bar crest location quantified from time-averaged X-band radar images. *Coastal Engineering* **45**: 19–32.

Ruessink BG, Coco G, Ranasinghe R, Turner IL. 2007. Coupled and noncoupled behavior of three-dimensional morphological patterns in a double sandbar system. *Journal of Geophysical Research: Oceans* **112**: C07002. https://doi.org/10.1029/2006JC003799.

Ruessink BG, Pape L, Turner IL. 2009. Daily to interannual cross-shore sandbar migration: observations from a multiple sandbar system. *Continental Shelf Research* **29**: 1663–1677.

Short AD. 1978. Wave power and beach stages: a global model. In *Proceedings of Coastal Engineering*, Am. Soc. of Civ. Eng., New York; 1145–1162.

Sonu CJ. 1973. Three-dimensional beach changes. *Journal of Geology* **81**: 42–64.

Splinter KD, Holman RA, Plant NG. 2011. A behavior-oriented dynamic model for sandbar migration and 2DH evolution. *Journal of Geophysical Research: Oceans* **116**: 1–21.

Stewart CJ, Davidson-Arnott RGD. 1988. Morphology, formation and migration of longshore sandwaves; Long Point, Lake Erie, Canada. *Marine Geology* **81**: 63–77.

Stive MJF, De Schipper MA, Luijendijk AP, Aarninkhof SGJ, Van Gelder-Maas C, Van Thiel de Vries JSM, De Vries S, Henriquez M, Marx S, Ranasinghe R. 2013. A new alternative to saving our beaches from sea-level rise: the Sand Engine. *Journal of Coastal Research* **290**: 1001–1008.

Thiébot J, Idier D, Garnier R, Falqués A, Ruessink BG. 2012. The influence of wave direction on the morphological response of a double sandbar system. *Continental Shelf Research* **32**: 71–85.

Thornton EB, Humiston RT. 1996. Bar/trough generation on a natural beach. *Journal of Geophysical Research* **101**: 12097–12110.

Thornton EB, MacMahan J, Sallenger AHJ. 2007. Rip currents, mega-cusps, and eroding dunes. *Marine Geology* **240**: 151–167.

Tiessen MCH, Dodd N, Garnier R. 2011. Development of crescentic bars for a periodically perturbed initial bathymetry. *Journal of Geophysical Research* **116**: F04016. https://doi.org/10.1029/2011JF002069.

Van de Lageweg WI, Bryan KR, Coco G, Ruessink BG. 2013. Observations of shoreline–sandbar coupling on an embayed beach. *Marine Geology* **344**: 101–114.

Van Enckevort IMJ, Ruessink BG. 2001. Effect of hydrodynamics and bathymetry on video estimates of nearshore sandbar position. *Journal of Geophysical Research* **106**: 16969–16979.

Van Enckevort IMJ, Ruessink BG. 2003. Video observations of nearshore bar behaviour. Part 2. Alongshore non-uniform variability. *Continental Shelf Research* **23**: 513–532.

Van Enckevort IMJ, Ruessink BG, Coco G, Suzuki K, Turner IL, Plant NG, Holman RA. 2004. Observations of nearshore crescentic sandbars. *Journal of Geophysical Research: Oceans* **109**. https://doi.org/10.1029/2003JC002214.

Van Enckevort IMJ, Wijnberg KM. 1999. Intra-annual changes in bar plan shape in a triple bar system. In *Proceedings of Coastal Sediments*, Am. Soc. of Civ. Eng., New York; 1094–1108.

Van Rijn LC, Walstra DJR, Grasmeijer B, Sutherland J, Pan S, Sierra JP. 2003. The predictability of cross-shore bed evolution of sandy beaches at the time scale of storms and seasons using process-based profile models. *Coastal Engineering* **47**: 295–327.

Wijnberg KM, Terwindt JHJ. 1995. Extracting decadal morphological behaviour from high-resolution, long-term bathymetric surveys along the Holland coast using eigenfunction analysis. *Marine Geology* **126**: 301–330.

Wong PP, Losada IJ, Gattuso JP, Hinkel J, Khattabi A, McInnes KL, Saito Y, Sallenger A. 2014. Coastal systems and low-lying areas. In *Climate Change 2014: Impacts, Adaptation and Vulnerability. Part A: Global and Sectoral Aspects Contribution of Working Group II to the Fifth Assessment Report of the Intergovernmental Panel on Climate Change*, Field CB, Barros VR, Dokken DJ, Mach KJ, Mastrandrea MD, Bilir TE, Chatterjee M, Ebi KL, Estrada YO, Genova RC, Girma B, Kissel ES, Levy AN, MacCracken S, Mastrandrea PR, White L (eds), Cambridge University Press: Cambridge, UK; 361–409.

Wright LD, Short AD. 1984. Morphodynamic variability of surf zones and beaches: a synthesis. *Marine Geology* **56**: 93–118.